Driving potential and noise level determine the synchronization state of hydrodynamically coupled oscillators
Supplementary material

Nicolas Bruot,[1] Jurij Kotar,[1] Filippo de Lillo,[2,3] Marco Cosentino Lagomarsino,[4,2] and Pietro Cicuta[1]

[1] *Cavendish Laboratory and Nanoscience Centre, University of Cambridge, Cambridge, U. K.*
[2] *Dipartimento di Fisica, Università di Torino, Torino, Italy*
[3] *DICAT, Università di Genova, Genova, Italy*
[4] *Genomic Physics Group, UMR 7238 CNRS "Microorganism Genomics", University Pierre et Marie Curie, Paris, France*

S.1. INTRODUCTION

This supplementary material provides details of the calculations estimating the fluctuations of the delay time t_1 and the average value of the synchronization order parameter Q, together with additional simulations performed with various functional forms of the potential. It also gives some technical details on how the experimental data on a single flagellum of *Chlamydomonas* from [1] has been processed in order to match the model and estimate the expected state of synchronization.

The supplementary material is organized as follows. In section S.2, we give details on the driving potentials used in the simulations and in the experiments. In section S.3, first a derivation of the evolution equation for the delay time t_1 in absence of noise. Then the effect of noise on t_1 is considered, allowing to derive estimates for (a) the distribution of Q and (b) the average $\langle Q \rangle$. In section S.4 simulations are presented that justify the choice of the "curvature" parameter c as a control parameter for the transition of synchronization states. Finally in section S.5 details are given for the model-guided analysis of the *Chlamydomonas* biological organism data.

S.2. DRIVING POTENTIALS IN SIMULATIONS AND EXPERIMENTS

A. Simulations

The force $F_i(x_i, t)$ used in the simulations is given by

$$F_i(x_i, \sigma_i(t)) = -\sigma_i \alpha k_\alpha \left| x + \sigma_i \frac{\lambda}{2} \right|^{\alpha - 1} . \tag{S1}$$

Here, $\sigma_i = \pm 1$ is the state of the switch acting on bead i and defines in which direction F_i is dragging the bead, and x_i is measured from the mean position. λ is the distance between the centers of the two traps driving one of the beads. The geometric switch imposes a constant amplitude of oscillations $A = \lambda - 2\varsigma$. The trap stiffness k_α is chosen such that the period of oscillation stays constant when changing the value of α. A straightforward calculation (for a single oscillator and neglecting the noise) gives:

$$k_\alpha \; = \; \frac{2\gamma}{T_0} \frac{1}{\alpha(2-\alpha)} \left[(A + \varsigma)^{2-\alpha} - \varsigma^{2-\alpha} \right] , \tag{S2}$$

where T_0 is the period of a single oscillator (set to $T_0 = 0.427s$ to match experiments).

B. Experiments

Experimental potentials are not power laws – they are smooth and have a clear curvature, but do not have the shape of a particular analytical function. Potentials for a single bead are realized by time-sharing of a single laser beam: The laser beam scans at a 20 kHz rate about 50 different positions along a line of direction x. Along this line, the intensity of the beam is changed depending on the position. This is realized experimentally by using acousto-optic deflectors. Consequently, the bead feels a potential that is harmonic in the y direction and of a shape depending on the laser intensity landscape along x. By setting three different intensity landscapes, we generated the three potentials shown in Fig. 1(b). These measured potentials are then used to calculate a corresponding curvature that can be used in the theoretical model and in comparison with simulations.

S.3. DERIVATION OF $\langle Q \rangle$

A. Evolution of t_1 without noise, and synchronized states

The calculation is based on the simplifying assumption that the potentials are composed of two linear sections (two slopes). For one single bead, and considering the origin of the positions $x = 0$ in the middle of the two geometric switching conditions, this "two-slopes" potential (the purple lines in Fig. 1(c) of the main text) can be characterized by the driving force

$$F(x) = \begin{cases} \sigma F_b & \text{if } \sigma x > \frac{A}{2} - x_0 \\ \sigma F_e & \text{otherwise.} \end{cases} \tag{S3}$$

Here $\sigma = \pm 1$ is the state of the geometric switch, A the amplitude (see Fig. 1 of the main text), and x_0 is a parameter that describes at what position the force will switch between $\pm F_b$ and $\pm F_e$. In other words, the bead is driven by a force $\pm F_b$ just after a geometric switch, until it moves a distance x_0 far from the switch position. Then the force becomes $\pm F_e$, until the next geometric switch.

For two beads, the equation of motion, Eq. (2) in the main text, can be written (without noise) as:

$$\begin{cases} \dot{x}_1 = \frac{1}{\gamma} F_1(x_1, t) + \epsilon \dot{x}_2 \\ \dot{x}_2 = \frac{1}{\gamma} F_2(x_2, t) + \epsilon \dot{x}_1 \ , \end{cases} \tag{S4}$$

where $\epsilon = \frac{3a}{2d}$ quantifies the strength of the hydrodynamic coupling coefficient between bead 1 and 2. Between geometric switches, or "slope break"[7] events, the forces are constant and the system is solved immediately ($F_1 = \pm F_u$ and $F_2 = \pm F_v$ with $u, v \in \{`b', `e'\}$). The velocities of the beads are

$$\begin{cases} \dot{x}_1 = \frac{1}{\gamma(1-\epsilon^2)} \left(F_u + \epsilon F_v \right) \\ \dot{x}_2 = \frac{1}{\gamma(1-\epsilon^2)} \left(F_v + \epsilon F_u \right) \end{cases} . \tag{S5}$$

In order to advance, one needs to assume an order in which geometric switches and slope breaks occur. Two general cases need to be considered. These are sketched in Fig. S1 and correspond to oscillations that are almost in phase or almost in antiphase. In both cases, each half-cycle is split into four pieces, for which the forces are constant and lead to velocities given by Eq. (S5). The half-cycle can be expressed as a linear system of eight equations describing the position of each of the two beads in the four parts, depending on the times t_1 to t_4, t_1' and the distances δ_1 to δ_4 (see notations in Fig. S1). For the case of configurations close to in-phase motion (Fig. S1(a)), the linear system is

$$\begin{cases} \delta_1 &= \frac{1}{\gamma(1-\epsilon^2)}(F_b - \epsilon F_e) t_1 \\ \delta_2 &= \frac{1}{\gamma(1-\epsilon^2)}(F_b + \epsilon F_b) t_2 \\ x_0 - \delta_1 &= \frac{1}{\gamma(1-\epsilon^2)}(F_b + \epsilon F_b) t_2 \\ x_0 - \delta_2 &= \frac{1}{\gamma(1-\epsilon^2)}(F_b + \epsilon F_e) t_3 \\ A - x_0 - \delta_3 &= \frac{1}{\gamma(1-\epsilon^2)}(F_e + \epsilon F_b) t_3 \\ A - x_0 - \delta_4 &= \frac{1}{\gamma(1-\epsilon^2)}(F_e + \epsilon F_e) t_4 \\ \delta_3 &= \frac{1}{\gamma(1-\epsilon^2)}(F_e + \epsilon F_e) t_4 \\ \delta_4 &= \frac{1}{\gamma(1-\epsilon^2)}(F_e - \epsilon F_b) t_1' \end{cases} \tag{S6}$$

This set of equations can be solved to find a discrete evolution map for the time delay t_1' after a half cycle, depending on t_1.

$$t_1' = \kappa_P t_1 \tag{S7}$$

with

$$\kappa_P = \frac{F_e + \epsilon F_b}{F_e - \epsilon F_b} \frac{F_b - \epsilon F_e}{F_b + \epsilon F_e}. \tag{S8}$$

t_1 is a proxy for the phase difference between the two oscillators, and is zero when they are synchronized. If the considered half-cycle is the k-th, $t_1 = t_1^{(k)}$, $t_1' = t_1^{(k+1)}$, giving the equation of evolution found in the main text, which predicts in-phase synchronization for $\kappa_P < 1$ with a characteristic relaxation time $1/\kappa_P$ (in half-cycles). It is interesting to note that this equation does not depend on the geometric parameter x_0 that appears in the definition

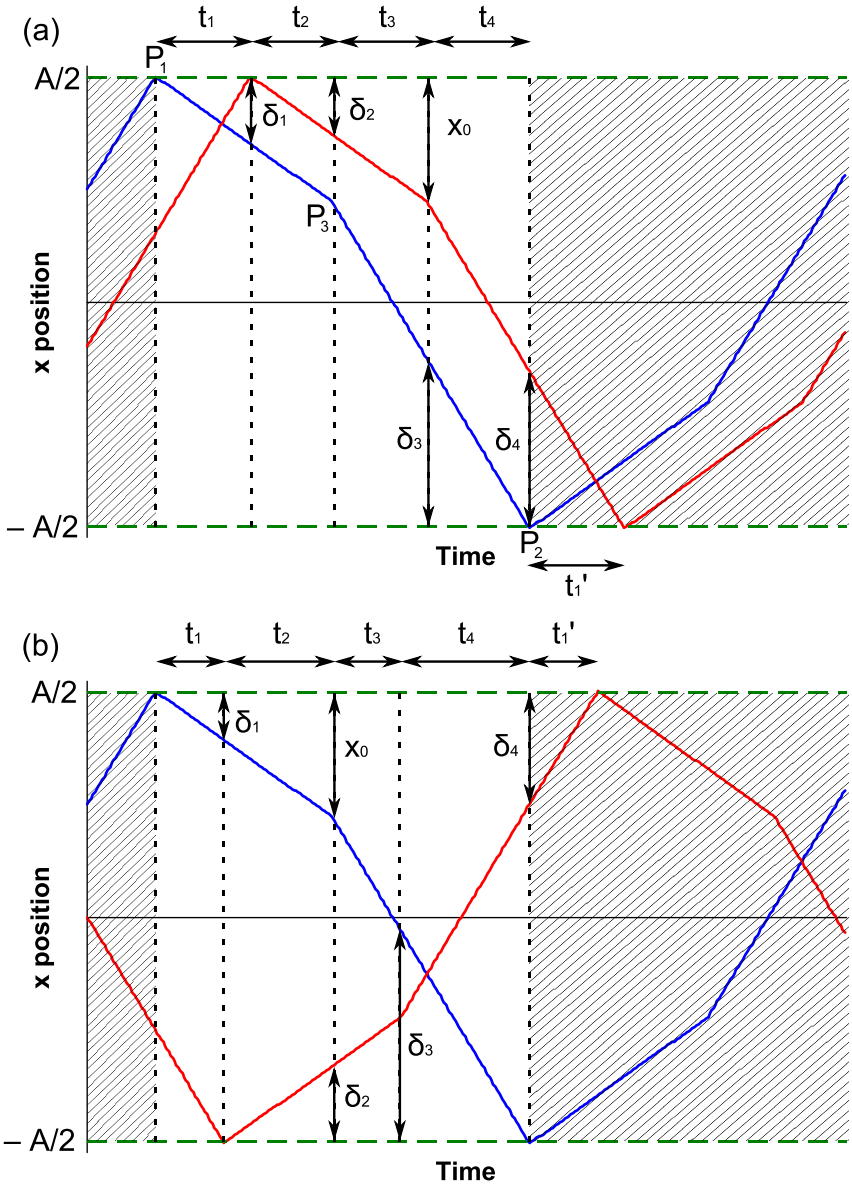

FIG. S1: Schematics and parameters of a half-cycle dynamics in the two-slope approximation. A generic potential is approximated by a two-slopes linear potential, leading to piecewise constant bead velocities. The time t_1 is estimated by considering two possible half-cycles: (a) for oscillations close to in-phase motion and (b) for oscillations close to antiphase. For simplicity, the slopes breaks in the position of one bead due to geometric switches or $F_b \to F_e$ switches of the other bead are not displayed here, but are taken into account in the calculation. The simplicity of our model allows to obtain the time t_1' depending on t_1, even when noise is added to the system.

of the potential. Only the driving forces near the geometric switches need to be considered. However, the solution assumes that the oscillations are described by a cycle as sketched in Fig. S1(a), which makes the equations invalid for large t_1, or x_0 close to 0 or to A. This approximation can explain the discrepancy between theoretical estimate and simulations in Fig. 4 of the main text. The effect of the parameter x_0 on the transition is discussed in section S.4 A.

The corresponding map for t_1 for the case of oscillations that are almost in antiphase can be obtained from the previous result by noting that the interaction of the second particle on the the first one is the same but with an opposite sign. Therefore, κ_{AP} is the same as κ_P but with ϵ replaced by $-\epsilon$:

$$\kappa_{AP} = \frac{F_e - \epsilon F_b}{F_e + \epsilon F_b}\frac{F_b + \epsilon F_e}{F_b - \epsilon F_e}. \tag{S9}$$

While not formally necessary here, both the perturbations with respect to a synchronized state and ϵ can be considered to be small parameters [2, 3]. The above expressions for κ_P and κ_{AP} can then be easily recast in the expressions given in the main text by expanding in ϵ to first order.

B. Effect of the noise on t_1

Starting from an initial condition t_1, the noise will affect t_1' by modifying the arrival times of the beads at each geometric switch or slope break. As each half-cycle is composed of four parts, this is in principle a complex, coupled first-passage time (FPT) problem. In our analytical estimates of the effect of noise, in order to make the problem tractable, we neglect the coupling between the two beads, so that the two beads can be treated separately (we remind the reader that the full model is solved numerically). Without coupling, the half-cycle of the blue bead in Fig. S1(a) is made of two parts. Starting from a position $A/2$ (point P_1), the position decreases at a velocity $-v_b = -F_b/\gamma$ during a time $t_1 + t_2$, until the bead reaches the point P_3 (defined by its position $A/2 - x_0$), where the velocity will become $-v_e = -F_e/\gamma$. The position continues to decrease for a time $t_3 + t_4$ until the end of the half-cycle (point P_2, position $-A/2$). The first part is a simple FPT problem and the distribution of the arrival time $t_1 + t_2 = t$ is given by the probability density [4]:

$$P_{\mathrm{FPT}_1}(t) = \frac{1}{\sqrt{4\pi D t^3}} \mathrm{e}^{-\frac{(x_0 - v_b t)^2}{4Dt}} \ . \tag{S10}$$

The second part is also described by a similar FPT distribution, except that when starting after point P_3, the bead can go backwards and spend some time in a potential corresponding to the previous velocity $-v_b$. This effect is likely happening just after P_3, during a time t_c defined as $v_e t_c = \sqrt{2Dt_c}$ which represents the possibility that the noise pushes the bead back towards the position $A/2 - x_0$ despite the average tendency to move at velocity $-v_e$. The effect is negligible when $t_c \ll \langle t_3 + t_4 \rangle$, or equivalently $2D/v_e \ll A - x_0$. For a choice of x_0 and c such that the quantity $A - x_0$ is of the same order of magnitude as A, and v_e is of the same order of magnitude as $v_0 = F_0/\gamma$, this condition is equivalent to $\xi \ll 1$ where $\xi = 2D/(Av_0)$ is a dimensionless expression of the noise strength. In this case, the distribution of $t_3 + t_4 = t$ is well-approximated by

$$P_{\mathrm{FPT}_2}(t) = \frac{1}{\sqrt{4\pi D t^3}} \mathrm{e}^{-\frac{(A - x_0 - v_e t)^2}{4Dt}}. \tag{S11}$$

When $\xi \ll 1$, the distributions P_{FPT_1} and P_{FPT_2} can also be approximated by Gaussians. In this case, the random variable $t_1 + t_2 + t_3 + t_4$ is described by a Gaussian distribution, of mean value $x_0/v_b + (A - x_0)/v_e$ and variance

$$2D \left(\frac{x_0}{v_b^3} + \frac{A - x_0}{v_e^3} \right). \tag{S12}$$

Fig. S2 shows simulations comparing this approximated probability distribution with models using power-law potentials as well as with direct simulation of the two-slopes model. The effect of varying the value of x_0 is also discussed.

The difference of the arrival times of the two beads t_1 can be written as:

$$t_1' = \kappa t_1 + \zeta \tag{S13}$$

with ζ a random variable accounting for the noise. At the general k-th step:

$$t_1^{(k+1)} = \kappa t_1^{(k)} + \zeta(k), \tag{S14}$$

with $\kappa = \kappa_P$ or κ_{AP} depending on the sign of c and $\zeta(k)$ a Gaussian random variable characterized by

$$\langle \zeta \rangle = 0 \tag{S15}$$

and

$$\langle \zeta^2 \rangle = 4D \left(\frac{x_0}{v_b^3} + \frac{A - x_0}{v_e^3} \right). \tag{S16}$$

The extra factor 2 compared to Eq. (S12) accounts for the summation of the variances of each of the two beads.

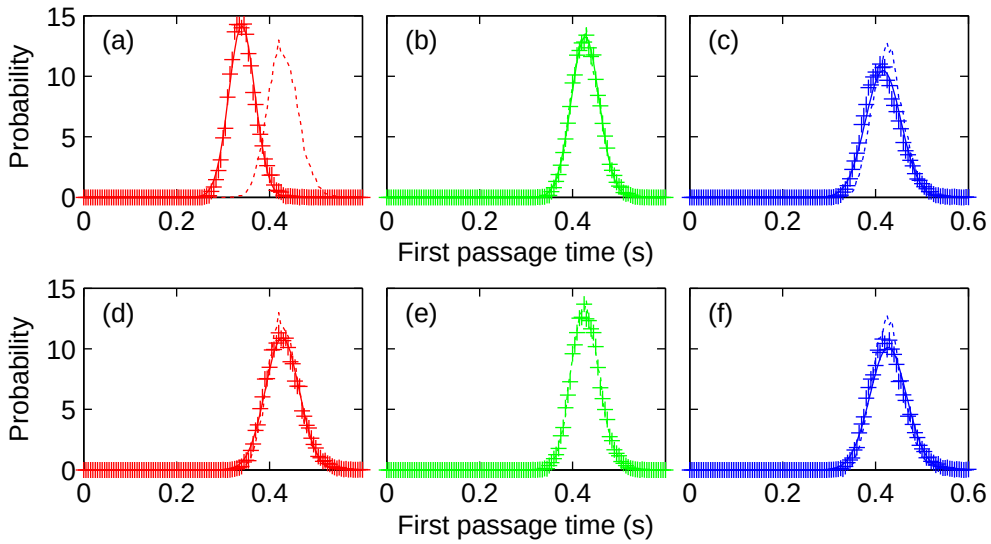

FIG. S2: First passage time distributions for different values of the parameter c: -0.42 (red), 0 (green) and 0.42 (blue). (a,b,c) For each c, three distributions are compared, coming form a simulation with a power-law potential (dashed line), a simulation of the corresponding two-slopes model (+ markers) and the approximating Gaussian distribution Eq. (S12) (solid line). In the two-slopes model, F_b and F_e are chosen such as they match the values of the force of the power law potential at the geometric switches and x_0 satisfies $x_0/v_b = (A - x_0)/v_e$. In (d,e,f), we compare the FPT from power law potentials (+) with two-slopes potentials (dashed lines) and its theoretical distribution (plain lines) for which x_0 is chosen such as the deterministic period is the same in all the potentials. The distributions in (d,e,f) fit very well. However, in order to keep the calculation of $\langle Q \rangle$ simple and reduce the number of parameters, we used the two-slopes model displayed in (a,b,c). In this case, for highly negative values of c (worst case in (a)), the average value of the FPT of the power law potentials differ from the two-slopes model by 30 %. However, in the definition of $\langle Q \rangle$ (equation (S28)), the relevant quantity to estimate is the ratio $\langle |t_1| \rangle / \langle \tau \rangle \propto \mathrm{std}(t_1)/\langle t_1 \rangle$. Between simulations with power law potentials and with the two-slopes model, this quantity differs only by 6 % in (a), 3 % in (b) and 15 % in (c). Parameters: $a = 1.735$ μm, $\eta = 2.21$ mPa·s, $T = 296$ K, $A = 3.12$ μm, $L = 1$ μm, $\alpha = 0.37$ (red), 1 (green) and 1.63 (blue).

ζ characterizes the fluctuations of t_1 that need to be added at each half-cycle of oscillation. The fluctuations of the steady state $t_1^{(\infty)}$ are given by iterating equation (S14) as in [2], leading to the following estimates for the first two moments of the $t_1^{(\infty)}$ random variable (assumed Gaussian)

$$\left\langle t_1^{(\infty)} \right\rangle = 0 \tag{S17}$$

and

$$\left\langle \left(t_1^{(\infty)} \right)^2 \right\rangle = \frac{1}{1-\kappa^2} \left\langle \zeta^2 \right\rangle . \tag{S18}$$

From here on, we take a simplifying assumption for x_0 and impose that the two-slope potential satisfies the condition $x_0/v_b = (A - x_0)/v_e$. This means that, in the absence of coupling, a bead would spend on average an equal time in the high-gradient and low-gradient potential steps. A consequence is that the average period of oscillation becomes $2A/v_0$ and does not depend on c. Note that the choice of x_0 is arbitrary, provided that it is chosen within a "reasonable" range. Namely, that the "v_b to v_e" switch at x_0 happens far away from the geometric switches in order to satisfy first that the oscillations stay in a cycle described either as (a) or (b) in Fig. S1, and second that the approximation of t_1 as a Gaussian random variable is stay valid. This choice of x_0 does not give the best two-slope estimate (see Fig S2), but is convenient to keep the algebra simple and obtain closed expressions.

Additionally, we introduce the approximation that the coupling term ϵ is small, so that κ can be expanded to the first order in ϵ. Including both assumptions in the noise on $t_1^{(\infty)}$ leads to the simplified expression:

$$\rho^2 = \left\langle \left(t_1^{(\infty)} \right)^2 \right\rangle = \left(\frac{A}{v_0} \right)^2 \frac{1+c^2}{1-c^2} \frac{\xi}{8\,|c|\,\epsilon}. \tag{S19}$$

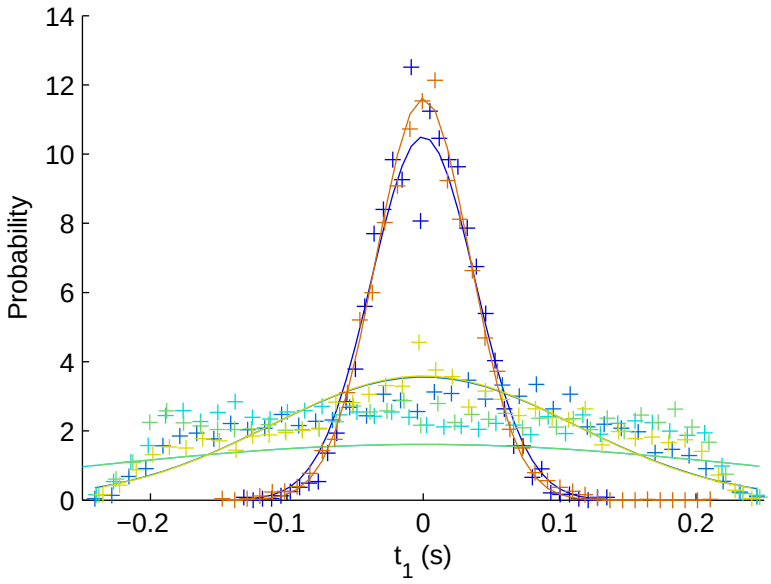

FIG. S3: Numerical distributions of the times t_1 for different values of c (0.42, 0.035, 0.0071, -0.0071, -0.035 and -0.42 from blue to orange). Even for high values of $|c|$, the distributions are in very good agreement with the analytical estimate (solid lines).

The absolute value ensures that this formula is valid for both $c > 0$ and $c < 0$. Fig. S3 shows distributions of t_1, corresponding to the simulations presented in the main text. The simulations agree very well with the approximated Gaussian distribution obtained above.

C. Probability distribution of Q

We estimated the probability distribution of the synchronization order parameter Q, given in Fig. 3 of the main text, within the assumption that $x_0/v_b = (A - x_0)/v_e$. From its definition in the main text, the parameter Q can be expressed piecewise for negative and positive values of c as a function of $|t_1|$:

$$Q(k) = \begin{cases} 1 - 2\frac{|t_1(k)|}{\tau_P(k)} & \text{if } c < 0 \\ -1 + 2\frac{|t_1(k)|}{\tau_{AP}(k)} & \text{if } c > 0 \end{cases} . \tag{S20}$$

Here, $\tau_P(k)$ (or τ_{AP} if $c > 0$) is the duration of the half-cycle k. Its expression at the first order in ϵ is:

$$\tau_P(k) = t_{1,P}(k) + t_{2,P}(k) + t_{3,P}(k) + t_{4,P}(k) \tag{S21}$$

$$= (1 - \epsilon)\frac{A}{v_0} + 2\epsilon\left(1 + \frac{2c}{1 - c^2}\right)\left|t_1^{(k)}\right| . \tag{S22}$$

For positive "curvatures" c, $\tau_P(k)$ has to be replaced by τ_{AP}, for which ϵ is changed to $-\epsilon$. The in-phase and anti-phase periods differ slightly, so the cycle average $\langle Q \rangle$ is not identical to a time average, accounting for the offset of $\langle Q \rangle_k$ at $c = 0$ in Fig. 3 of the letter.

In order to obtain the distribution of Q, we need the probability distribution of $t' = \left|t_1^{(\infty)}\right|$. As we assume $t_1^{(\infty)}$ is Gaussian random variable, t' follows the half-normal distribution

$$P_a(t) = \sqrt{\frac{2}{\pi\rho^2}} \exp\left(-\frac{t^2}{2\rho^2}\right) . \tag{S23}$$

The probability distribution of Q_P, $P_{Q_P}(q)$, is then deduced from Eq. (S23) and Eq. (S20)

$$P_{Q_P}(q) = \left|\frac{\mathrm{d}}{\mathrm{d}q} Q_P^{-1}(q)\right| P_a(Q_P^{-1}(q)) \tag{S24}$$

leading to:

$$P_{Q_P}(q) = P_a\left(\frac{A}{v_0}\frac{1-q}{B+K(1-q)}\right)\frac{B}{\left(B+K(1-q)\right)^2} \tag{S25}$$

where

$$\begin{cases} B &= \frac{2}{1-\epsilon} \\ K &= \frac{-2\epsilon}{1-\epsilon}\left(1+\frac{2c}{1-c^2}\right) \end{cases}. \tag{S26}$$

$P_{Q_{AP}}$ is obtained similarly and results in the same formula, but with ϵ replaced by $-\epsilon$ in the expressions of the parameters B and K. P_{Q_P} and $P_{Q_{AP}}$ are represented in Fig. 3(d) of the main text.

D. Order parameter $\langle Q\rangle$

As $|t_1|$ appears both in the numerator and denominator in Eq. (S20), the exact probability distribution of Q is hard to derive. To keep the calculation simple, we replace in Eq. (S20) $\tau_P(k)$ by $\langle\tau_P\rangle + u(k)$ and make a Taylor expansion of the denominator, leading, for $c<0$, to:

$$Q(k) = 1 - 2\frac{|t_1(k)|}{\langle\tau_P\rangle}\left(1-\frac{u(k)}{\langle\tau_P\rangle}+\left(\frac{u(k)}{\langle\tau_P\rangle}\right)^2+\dots\right). \tag{S27}$$

When taking the average $\langle Q\rangle$, the first correction term is $\mathrm{var}(u(k))/\langle\tau_P\rangle^2 \sim \mathrm{var}(t_1)/\langle\tau_P\rangle^2$. It is negligible when both $\epsilon \ll 1$ and $\xi\epsilon/|c| \ll 1$. At room temperature and with our experimental parameters, $\xi = 4.96\times10^{-3}$ and $\epsilon = 0.26$, and the correcting term can be dropped for all curvatures except in the tiny range $|c| < 10^{-3}$. This simplification leads to the expression of $\langle Q\rangle$ plotted in Fig. 3(a) of the paper

$$\langle Q\rangle = \begin{cases} 1-2\frac{\langle|t_1|\rangle}{\langle\tau_P\rangle} & \text{if } c<0 \\ -1+2\frac{\langle|t_1|\rangle}{\langle\tau_{AP}\rangle} & \text{if } c>0 \end{cases} \tag{S28}$$

$$= \begin{cases} 1-\frac{\alpha}{\sqrt{\epsilon}}\left(1-\beta\sqrt{\epsilon}+\left(\beta^2+1\right)\epsilon\right) & \text{if } c<0 \\ -1+\frac{\alpha}{\sqrt{\epsilon}}\left(1+\beta\sqrt{\epsilon}+\left(\beta^2-1\right)\epsilon\right) & \text{if } c>0 \end{cases} \tag{S29}$$

where

$$\alpha = \sqrt{\frac{\xi}{\pi|c|}\frac{1+c^2}{1-c^2}} \tag{S30}$$

and

$$\beta = \left(1+\frac{2c}{1-c^2}\right)\alpha. \tag{S31}$$

Note that $\langle Q\rangle$ diverges when c tends to 0, since α tends towards ∞. In fact, κ tends to 1 in that case, and the phase of the two particles becomes free. Our initial assumption that the cycle could be described by Fig. S1(a) for $c<0$ and Fig. S1(b) for $c>0$ fails in that particular case. This is however happening in a small range of c for moderate noise levels.

S.4. ADDITIONAL CONTROL SIMULATIONS

A. Simulated two-slopes model

In our estimation of the effect of the noise on the P/AP transition, the two-slopes model required the use of the parameter x_0 which defines at what position the potential switches from F_b to F_e. We already showed that this parameter does not affect the relaxation time $1/\kappa$, at least at small levels of noise. However, it does appear in the calculation of the half-period τ of oscillations, and therefore $\langle Q\rangle$. Fig. S4 displays simulations of the transition by using two-slopes potentials for different values of x_0. It appears that, except for values of x_0/A close to 0 or 1, the shape of the transition is always the same. When x_0/A approaches 0 or 1, we explain the changes in the transition as a failure to apply the approximation on the shape of the cycle: the slope breaks occur so close to the geometric switches that the cycle cannot be described as in Fig. S1(a or b).

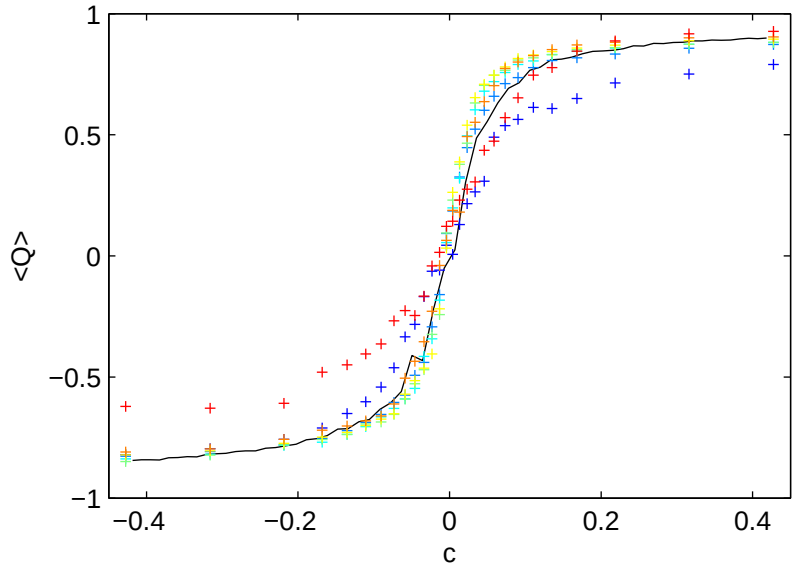

FIG. S4: $\langle Q \rangle$ transition for several values of x_0. x_0/A is 0.1, 0.25, 0.4, 0.5, 0.5, 0.6, 0.75 and 0.9 from blue to red. As a comparison, the black line is the transition from simulations obtained in the paper by using power laws. All the curves fit to the same transition except for values of x_0/A close to 0 or 1.

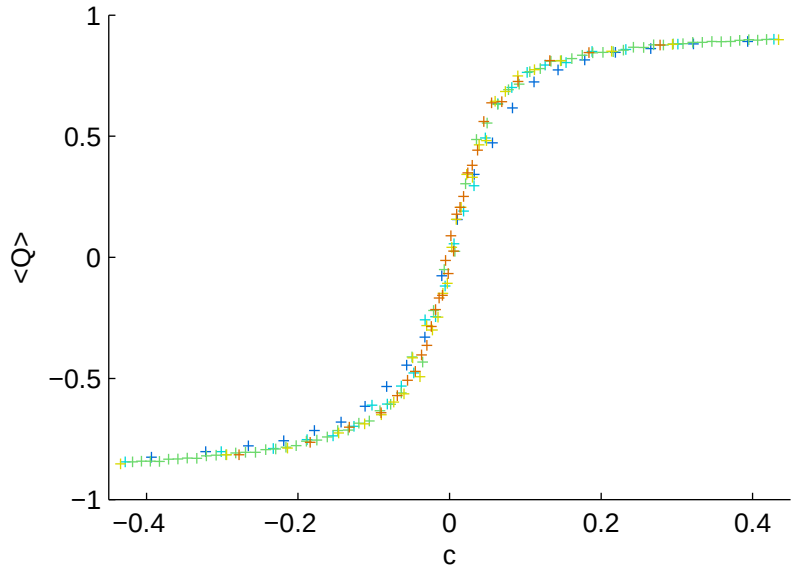

FIG. S5: $\langle Q \rangle$ transition for power-law potentials with several values of ς: A/ς is 0.94, 0.76, 0.61, 0.44 and 0.28 from blue to red. When ς is changed, λ is also modified in order to keep the amplitude constant between the different simulations. For each curve, c is changed through the parameter α and k_α is changed so that the average period of oscillations remains the same. All curves lead to the same transition.

B. Power law potentials with different values of ς

The simulated two-slopes model shows that the information on the whole shape of the potentials is not needed to describe the synchronized state. Only the forces F_b and F_e, from which the parameters F_0 and c are deduced, are relevant to the problem. As a complementary empirical proof of this assumption, we also performed simulations with power law potentials by varying both the parameter α, controlling c, and ς, which provides a way to change the whole shape of the potential (see Eq. (3) of the main text). Fig. S5 summarizes the different transitions obtained. For each curve, ς is constant and α is varied to change the "curvature" c. Again, all the curves fit remarkably well.

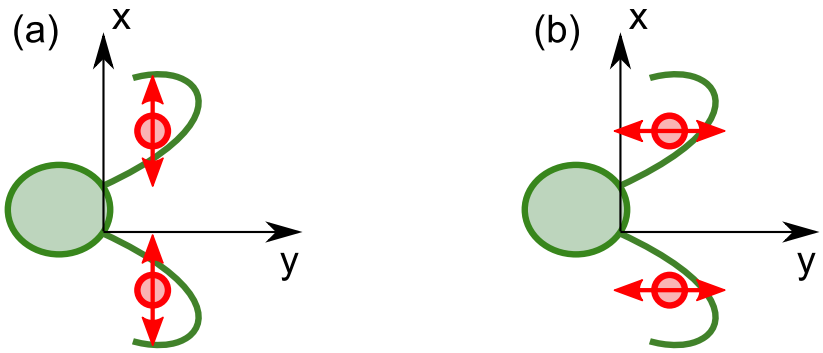

FIG. S6: This diagram is figure 3(e,f) from the main text, reproduced here for convenience. Each flagellum of *C. reinhardtii* is modeled by a rower (red sphere) oscillating along the direction shown by the red arrows. We studied two different cases: (a) oscillations transverse to the direction of propulsion and (b) oscillations in the direction of propulsion. We expect oscillations in antiphase in (a) and in phase in (b).

S.5. SYNCHRONIZATION OF THE TWO FLAGELLA IN *C. REINHARDTII*

This section describes how we used data of the force generated by a single flagellum of *Chlamydomonas* in order to match the model with experimental data concerning the synchronization of two flagella, and represented by the dashed line in Fig. 3(a) (insert) of the main text. Data on the position of a flagellum and the force exerted on it by the fluid during a cycle was kindly provided by Bayly and coworkers, and is the result of experimental image analysis from movies of an uniflagellated *Chlamydomonas* cell [1].

Our aim is to describe effectively the two flagella of a *Chlamydomonas* alga as two rowers, for which we expect from our work that the state of synchronization should be determined by the curvature of the potentials. An effective position of the flagellum and an effective driving potential need to be determined from the experimental data. In general, any attempt to reduce such a complex dynamics to a simple system is forcedly, at least to some extent, arbitrary. In our case, one main choice is how to decompose the beating motion into two one-dimensional oscillations.

When the flagella are synchronized, it is known that they beat most of the time in phase along the direction of propulsion and in anti-phase along the transverse direction [5]. We therefore considered two configurations of rowers which define two axes used for the projection of the position and force as shown in Fig. S6. From the effective potentials, we recover the expected synchronized state of the flagella (AP synchronization along the direction transverse to the swimming direction y) and justify that this axis leads to the main contribution to the synchronization. Section S.5 C also presents direct simulations of the two rowers oscillating in the extracted effective potentials that confirm our argument.

A. Computation of an effective potential

Fig. S7 shows processed data of the position of the flagellum and its force on the fluid. Reconstructing an effective potential acting on the flagellum requires the knowledge of the driving force field; this can be obtained from the data of position and driving force as a function of time. For the position, we simply take the centre of mass of the flagellum, which is represented by the red line in Fig. S7. For the driving force, we calculate the total force from the fluid acting on the flagellum, taking its opposite as $\mathbf{F}_{\text{tot}}$:

$$\mathbf{F}_{\text{tot}} = -\int_0^{s_0} f(s)\,\mathrm{d}s \tag{S32}$$

where $f(s)\,\mathrm{d}s$ is the force from the fluid acting on the small element of flagellum of length $\mathrm{d}s$, and s_0 the total length of the flagellum. This definition of the total force excludes the force from the body of the alga acting at the base of the flagellum, and explains why $\mathbf{F}_{\text{tot}}$ is not exactly tangential to the orbit of the centre on mass in Fig. S7.

The second step necessary to obtain data that can be used for rowers is to project the force along an axis. Synchronized states are described by a different locked phase depending on the axis of projection. As discussed above, we used the y (propulsion) and x (transverse) axes as these are the well-defined directions along which synchronized flagella can be said to be experimentally in phase or in antiphase. By considering for example the x projection, two

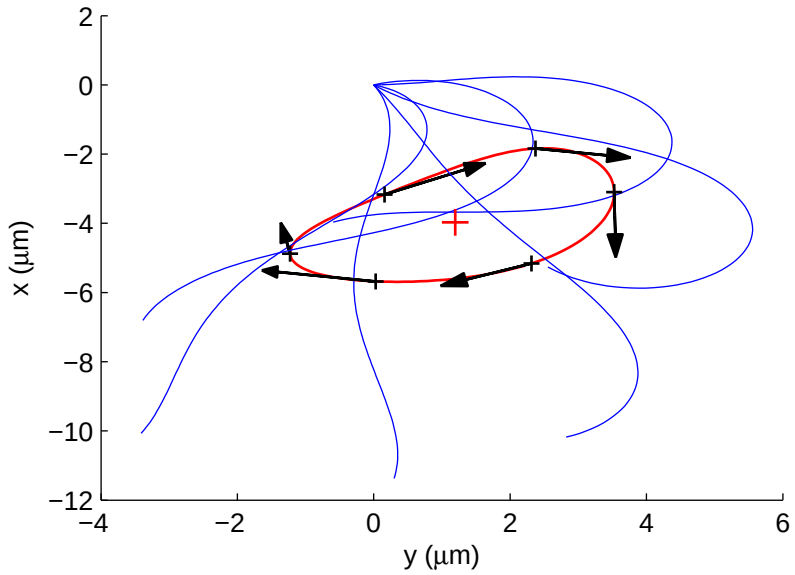

FIG. S7: Cycle of oscillation of a flagellum – In blue: flagellum at six different instants on the cycle. The motion of the centre of mass of the flagellum is represented by the red line. The opposite of the total force $\mathbf{F}_{\text{tot}}$ from the fluid on the flagellum (black arrows) is closely tangent to the motion of the centre of mass and is used to obtain the effective driving potential acting on the flagellum. The red marker is the average position of the centre of mass and is used to estimate the distance between the rowers.

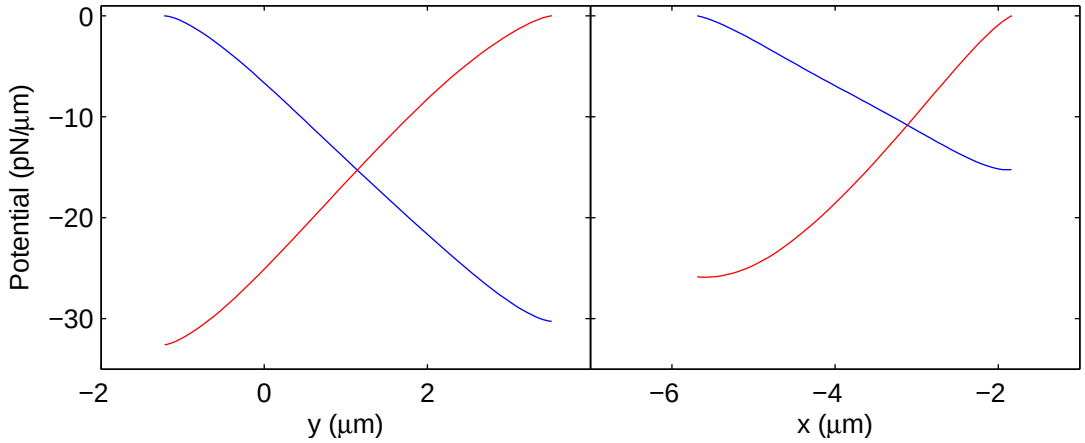

FIG. S8: Experimental effective potentials U_y^i, U_x^i (blue) and U_y^d and U_x^d (red) – The highest curvature is for U_x^d and is the main contribution to the synchronization of the two flagella.

values of the force are obtained for a given x: one for increasing x positions and one for decreasing positions

$$\begin{cases} F_x^i(x) = \mathbf{F}_{\text{tot}}(x) \cdot \hat{\mathbf{e}}_x & \text{for increasing } x \\ F_x^d(x) = \mathbf{F}_{\text{tot}}(x) \cdot \hat{\mathbf{e}}_x & \text{for decreasing } x \end{cases} . \tag{S33}$$

We therefore obtain two different potentials $U_x^i(x)$ and $U_x^d(x)$ for the motion along the x axis. The same analysis can be carried along the y direction. The effective potentials are represented in Fig. S8.

B. Synchronized state

The highest curvature appears in U_x^d. Furthermore, the coupling coefficient ϵ is $3a/(2d)$ in the configuration of rowers oscillating along x while it is only $3a/(4d)$ along y. Therefore, the model predicts that the main contribution

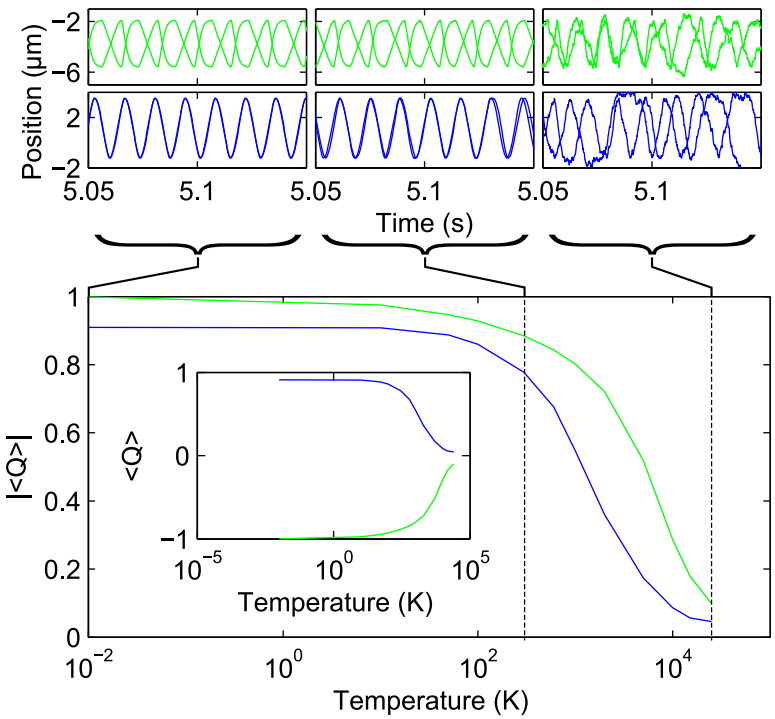

FIG. S9: Synchronization of two rowers under the effective potentials along the y (blue) and x (green) axes – The insert shows that at low temperature, the system is synchronized in phase along y and in antiphase along x, in agreement with experimental observations on *Chlamydomonas*. However, the main graph shows that for middle range temperatures (including room temperature), synchronization is stronger along the x direction.

to the synchronization of the two flagella comes from the oscillations along the x axis. Along this direction, U_x^d has a positive curvature while U_x^i has a small, negligible curvature. The model predicts synchronization in antiphase in this direction, in agreement with experimental observations.

C. Simulations of two rowers under effective potentials

As a control, the effective potentials of the previous section were used as an input to our Brownian Dynamics simulations of two rowers. The distance between the two rowers can be estimated by knowing (a) the average position of one of the flagellum in the data of Fig. S6 and (b) the distance between the bases of the two flagella of a *Chlamydomonas* alga. This distance has been estimated to 3 μm from the first snapshot of Fig. 2 in [6]. The (a) and (b) contributions lead to an average distance of 11 μm between the two rowers that model the flagella. The parameters in our simulations are $d = 10$ μm and $\eta = 10^{-3}$ mPa·s^{-1}. The switching positions are set to the extremes of the range of definition of the potentials in Fig. S8. Beyond this range of positions (i.e. overshooting the switch as can happen in the presence of noise), the driving forces are set to the value of the nearest position where the potential is defined in Fig. S8. The radius of the spherical rowers has been chosen so that the frequency of the simulated oscillations matches the experimental beat frequency of the flagellum. The radius is found to be the same for oscillations along x or y ($a = 0.45$ μm). This radius is in agreement with the resistive coefficient C_N in [1], the viscous friction coefficient $6\pi\eta a$ is equal (within 15 %) to the friction coefficient $4\pi\eta L/(\log(2q/r) + 0.5)$ with the notations and numerical values from [1]. Fig. S9 summarizes the results of our simulations, and confirms the results given in section S.5 C.

D. Where is *C. reinhardtii* on the noise/curvature phase diagram?

The position of *Chlamydomonas* in the phase diagram in Fig. 3(a) of the main text can now be estimated. The phase diagram is drawn for oscillations that are symmetric for decreasing and increasing positions. In the case of *Chlamydomonas*, for the data projected along y, only one of the two potentials is curved. During a cycle of oscillation, only one half of it will contribute to synchronization. However, thermal fluctuations are still present in both halves

of the cycle. In the non-symmetric system, we therefore estimated the noise parameter ξ by:

$$\xi = 2k_BT/(AF') \tag{S34}$$

where $F' = \gamma A/T_0$, with T_0 the period of oscillation, which leads approximately to a factor two compared to the definition of the main text. This definition avoids using F_b and F_e (through F_0) that are not the same for increasing and decreasing positions in the non-symmetric system. By this mean, ξ is estimated to 1×10^{-3} for the *Chlamydomonas* data.

The curvature c is harder to estimate, since the projection of the force along the orbit naturally gives forces that approach 0 rather smoothly at the assumed geometric switches [8]. In an attempt to obtain a value, we fitted the oscillation of a single rower at 0 K in the U_x^d potential with two slopes, with the slope break at a position such as $x_0/v_b = (A - x_0)/v_e$ with the notations of section S.3 B. This leads to the estimate $c \approx 0.75$.

[1] P. V. Bayly, B. L. Lewis, E. C. Ranz, R. J. Okamoto, R. B. Pless, and S. K. Dutcher, Biophys. J **100**, 2716 (2011).
[2] N. Bruot, L. Damet, J. Kotar, P. Cicuta, and M. Cosentino Lagomarsino, Phys. Rev. Lett. **107**, 094101 (2011).
[3] J. Kotar, M. Leoni, B. Bassetti, M. Cosentino Lagomarsino, and P. Cicuta, Proc. Natl. Acad. Sci. **107**, 7669 (2010).
[4] S. Redner, *A Guide to First-passage Processes* (Cambridge University Press, 2007), 1st ed., ISBN 0521036917.
[5] R. Goldstein, M. Polin, and I. Tuval, Phys. Rev. Lett. **103**, 168103 (2009).
[6] R. Goldstein, M. Polin, and I. Tuval, Phys. Rev. Lett. **107**, 148103 (2011).
[7] We call "geometric switch" a change of σ and a "slope break" a change of the absolute force from F_b to F_e (but not F_e to F_b, which occurs at a geometric switch).
[8] Exactly null forces would be found at the switches if the force field was exactly tangential to the orbit.